

Author Version: Ocean Dynamics, vol.67(7); 2017; 857-873

Interannual variability of zonal currents in the equatorial Indian Ocean: Respective control of IOD and ENSO

Chinnu Schidanandan¹, M. Lengaigne^{2,3}, P.M.Muraleedharan¹, Basil Mathew⁴

¹CSIR-National Institute of Oceanography (NIO), Goa, India

²Sorbonne Universités (UPMC, Univ Paris 06)-CNRS-IRD-MNHN, LOCEAN Laboratory, IPSL, Paris, France

³Indo-French Cell for Water Sciences, IISc-NIO-IITM-IRD Joint International Laboratory, NIO, Goa, India

⁴Npol,Thrakkakara,India

Corresponding author address

Dr.P.M.Muraleedharan

Physical Oceanography Division

National Institute of Oceanography

Dona Paula, Goa – 403 004

E- mail: mpm84521@gmail.com

Abstract

The observational record is too short to confidently differentiate the relative contributions of Indian Ocean Dipole (IOD) and El Niño/Southern Oscillation (ENSO) on the interannual variability of the equatorial current system in the Indian Ocean because of the strong tendency of these two modes to co-occur. In this study, we analyse a five-decade simulation from a ocean general circulation model forced to describe the main interannual variations of surface and subsurface equatorial zonal currents in the Indian Ocean. This simulation is first shown to accurately capture the surface and subsurface zonal currents variations in the equatorial region derived from the available observations. Through an EOF analysis on the model outputs, our results further reveals two main modes of equatorial currents interannual variability: a dominant mode with largest amplitude in fall largely describing the variability of the fall Wyrтки jet intensity followed a few months later by a secondary mode maximum in winter largely describing the interannual variability of the subsurface currents in that season. Our analysis further confirms that the IOD is largely responsible for the interannual modulation of fall Wyrтки jet intensity by modulating the equatorial wind intensity during that season. The IOD is also responsible for strong subsurface current variations until December, induced by the delayed effect of the IOD wind signal onto the equatorial thermocline tilt. The equatorial current system response to ENSO is weaker and delayed compared to that of the IOD. The remote and delayed impact of ENSO in the IO indeed induces equatorial wind variations in winter that modulate the winter surface currents intensity and the spring equatorial undercurrent intensity through its delayed impact on the thermocline tilt.

Keywords: Equatorial Undercurrent, Equatorial Jet, Inter-annual variability, Equatorial Indian Ocean, Indian Ocean Dipole, ENSO

Introduction

The dynamics of the tropical Indian Ocean (IO) is unique amongst the three tropical basins owing to the peculiar forcing induced by the seasonally reversing monsoon winds in this basin. Seasonally occurring equatorial eastward surface jets and westward Equatorial Undercurrents (EUC) are specific features of the IO equatorial current system. As shown on Figure 1a, the surface jets (also known as Wyrtki jets) occur twice a year during transition between summer and winter monsoons, i.e. in fall and spring inter-monsoon periods (e.g. Wyrtki 1973, Molinari et al. 1990; Reppin et al. 1999; Han and McCreary 1999; Yuan and Han 2006, Qiu et al. 2009). They are fully developed in the upper 100m in the central IO within the narrow equatorial belt and are mainly a direct response to the equatorial westerly wind forcing during the intermonsoon periods (e.g. O'Brien and Hurlburt 1974; Cane 1980; McPhaden 1982; Han et al. 1999; Fig. 1a). These jets modify the slope of the trans-equatorial thermocline by zonal redistribution of mass and volume transport on seasonal scales (McPhaden et al. 2015). Unlike the quasi-permanent EUC of Pacific and Atlantic, the equatorial current system in the IO exhibits seasonally transient EUCs (e.g. Knauss and Taft 1964; Bruce 1973), being driven by the seasonally varying component of surface wind over the central equatorial IO (Schott and McCreary 2001). This transient EUC pattern has been first reported during winter (typically from December to April) but can occasionally appear late summer/early fall period (August-October) with weaker intensities (Iskandar et al., 2009). The seasonal dynamics of these transient EUCs involve transient equatorial zonal winds and zonal pressure gradient. During winter, the prevailing easterly winds excite an upwelling equatorial Kelvin wave that drives an eastward pressure gradient at the origin eastward flow in the thermocline (Cane 1980; Clark and Liu 1993; Reppin et al. 1999). During summer, both the upwelling equatorial Kelvin wave triggered by summer easterlies and the downwelling Rossby waves generated by the reflection of the spring downwelling Kelvin waves in the eastern boundary contribute to the eastward pressure gradient and the generation of the summer EUC (Iskandar et al. 2009).

In addition to these seasonal variations, the equatorial wind system in the IO also undergoes strong interannual fluctuations. Two main climatic modes influence the interannual variability of wind and precipitation over the tropical Indian Ocean, namely the El Niño-Southern Oscillation (ENSO) and the Indian Ocean Dipole (IOD). ENSO originates in the tropical Pacific but remotely impacts the Indian Ocean by inducing anomalous subsidence there, resulting in a general warming of the basin (e.g. Klein et al., 1999). This warming lasts for two seasons after the peak of ENSO,

possibly maintained by local air–sea interactions over the Indian Ocean (e.g. Xie et al. 2009; Du et al. 2009). In addition to this basin-wide warming associated with ENSO, the tropical Indian Ocean is also home to another mode of variability, the IOD (e.g. Saji et al., 1999; Webster et al., 1999). Peaking earlier in boreal fall, it has a shorter lifetime than ENSO events, about six months. Its positive phase is associated with a well-defined cold anomaly along the coast of Java and Sumatra associated with a local suppression of convection there and anomalous easterlies over the central Indian Ocean. The strong easterlies along the equator and the southeasterlies along the coast off Sumatra and Java creates an anomalous anti-cyclonic curl that generate downwelling Rossby waves in south tropical IO during the developing phase of IOD (Rao and Behera 2005; Yu et al. 2005). These downwelling Rossby waves propagate into the western equatorial IO and deepen the thermocline thereby warming in the western equatorial IO (Murtugudde et al. 2000; Vinayachandran et al. 2002). IOD events are commonly triggered by ENSO events and frequently co-occur with them, yet they also occur independently and can hence be considered as an intrinsic mode of variability in the IO (e.g. Annamalai et al. 2003; Luo et al. 2010; Izumo et al. 2010, 2013).

The interannual wind stress fluctuations associated with these climate modes can directly contribute to interannual variations in the equatorial current system of this basin. Several studies reported large interannual variations in the intensity of the Wyrki jets (Reppin et al., 1999; Vinayachandran et al. 1999, 2007; Murtugudde et al. 2000; Grodsky et al. 2001; Han et al. 2004; Nagura and McPhaden 2010a; Gnanaseelan et al. 2012; Joseph et al. 2012) and the seasonal EUCs (Reppin et al. 1999; Iskandar et al. 2009; Swapna and Krishnan 2008; Nyadjro and McPhaden 2014) in response to interannual equatorial wind fluctuations. Easterly wind anomalies have been shown to reduce the intensity of the fall Wyrki jet (Han et al. 2004; Thompson et al. 2006; Nagura and McPhaden 2010a; Joseph et al. 2012). Interannual zonal current anomalies at the equator tends to lead the zonal wind stress anomalies by one month, as a response to the reflected Rossby waves radiating from the eastern boundary (Nagura and McPhaden 2010a). Easterly wind anomalies also intensify the EUC in late summer/early fall through an increase of the eastward pressure force in the thermocline (Han et al. 2004; Swapna and Krishnan 2008; Nyadjro and McPhaden 2014) and related off-equatorial southern hemisphere zonal winds that forces equatorward geostrophic thermocline flows (Krishnan and Swapna 2009; Zhang et al. 2014). Although recent studies generally focused on the equatorial current response to IOD forcing (Thompson et al. 2006; Swapna and Krishnan, 2008; Nagura and McPhaden 2010a; Joseph et al. 2012; Nyadjro and McPhaden, 2014; Zhang et al. 2014), it is difficult so far to disentangle the respective impact of IOD variations and ENSO on the IO equatorial current system because interannual variations of the equatorial winds are related to these

two climate modes which often co-occur. Such an attempt has been recently performed by Gnanaseelan et al. (2012) for the case of the surface Wyrki jet in fall. Their analysis suggest that both ENSO and IOD have a considerable impact on the IO surface currents, with IOD affecting currents throughout the equatorial IO and ENSO mainly affecting the eastern part of the basin.

In the present study, we aim at better assessing the respective influence of ENSO and IOD both on the surface and subsurface current system using a five-decade simulation from the ocean general circulation model. The paper is organised as follows. Section 2 provided a description of the in situ and model data. A comparison of the model and observed surface and subsurface currents at both seasonal and interannual timescales is further provided in Section 3. The main modes of interannual variability of surface and subsurface currents are presented in Section 4. Section 5 specifically separate out the respective contribution of ENSO and IOD on these interannual currents fluctuations. Section 6 finally provides a comprehensive summary and a comparison of the main outcomes of this paper with previously published literature.

1. Data and Method

1.1. Model dataset

The numerical simulation data used in this study is an output of DRAKKAR project (Brodeau et al. 2010). It is based on the NEMO (Nucleus for European Modelling of the Ocean) Ocean General Circulation Model with an eddy permitting $\frac{1}{4}^\circ$ horizontal resolution and 46 vertical levels with a 6-m spacing at the surface increasing to 250-m in the deep ocean. Bathymetry is represented with partial steps. The model is forced from 1958 to 2007 with the DFS3 dataset detailed in Brodeau et al. (2010). This forcing is essentially based on the corrected ERA-40 reanalysis (Uppala et al. 2005) before 2002 and ECMWF operational analysis beyond 2002 for near surface variables and corrected ISCCP-FD radiation product (Zhang et al. 2004) after 1984. The model simulation is initialized in 1958 with Levitus et al. (1998) climatology. Although ran from 1958, the simulation is analysed over the 1960-2007 period to allow the near equatorial ocean to spin-up over the first two years of the experiments.

This model forced with a similar forcing strategy is shown to successfully reproduce the variability over the Indian Ocean at a wide range of timescales (Nidheesh et al., 2012; Akhil et al., 2014, 2016; Vialard et al., 2013; Keerthi et al., 2013, 2016). A more detailed description of this simulation can be found in Nidheesh et al. (2013).

1.2. Observational datasets

Model currents are validated to in-situ velocity observations from upward looking Acoustic

Doppler Current Profilers (ADCP) in the equatorial IO. We will make use of the relatively long measurements from the RAMA (Research moored Array for African-Asia Australian Monsoon Analysis and Prediction; McPhaden et al. 2009) moorings in the eastern equatorial IO at 80.5°E (available from October 2004 to December 2007) and at 90°E (available from November 2000 to December 2007). The upward looking ADCP often generate random errors in the surface currents as they are contaminated by acoustic signals reflected off the surface. The model surface currents were hence also validated to the near surface real time velocity data from OSCAR (Ocean Surface Current Analyses Research) project available from November 1992 to present (Bonjean and Lagerloef 2002). Interannual signals for both model and observational datasets are calculated by removing the monthly climatology. A three months running mean is further applied on these anomalies to filter out intraseasonal signals.

We aim to assess the relationship between IO equatorial currents and known interannual climate modes in the Indian Ocean, i.e. the IOD and ENSO. To characterize these modes, we have used standard indices. In the Pacific, ENSO is classically represented by the mean sea surface temperature (SST) anomalies over the Niño3.4 (120°W-170°W; 5°N-5°S) region averaged from December to February. The IOD is represented by the dipole mode index (DMI, Saji et al. 1999) computed as the difference between interannual SST anomalies in the western (50°E-70°E; 10°N-10°S) and south-eastern equatorial Indian Ocean (90°E-110°E; 10°S-0°), averaged over the September–November season. These two indices were computed from the monthly HadISST dataset (Rayner et al. 2003). It must be noticed that these two indices are strongly correlated (~ 0.65), highlighting the tendency for ENSO and IOD to co-occur.

We also use a regression technique to extract patterns associated with each mode of climate variability over the IO. The use of standardized indices helps to provide these regressions values in physical units (e.g. $\text{m}\cdot\text{s}^{-1}$ for currents), which correspond to the “typical” anomalies associated with a positive IOD or ENSO event. But because of the strong correlation between some climate indices (e.g. a 0.65 correlation between IOD and ENSO indices), it is often difficult to separate the signals associated with each of those climate modes using a simple linear regression. Partial regression is hence used to isolate signals purely associated with, e.g. the IOD or ENSO. This computation requires three linear regressions. For example, if one wants to compute the partial regression between time series of currents (Cur_i) and the DMI index (D_i) independently of the ENSO index (E_i), one first subtract signals that are linearly related to (E_i) from (Cur_i) and (D_i) and perform a regression between the residuals as given below.

$$\text{Cur}_i = a \times E_i + \text{Cur}_e \quad \text{----- (4.1)}$$

$$D_i = b \times E_i + D_e \quad \text{----- (4.2)}$$

$$\text{Cur}_e = c \times D_e + M_{ed} \quad \text{----- (4.3)}$$

where Cur_e and D_e (in equations 4.1 and 4.2) are respectively the M_i and D_i residuals independent of ENSO. Equation 4.3 allows obtaining the partial regression coefficient c by regressing M_e onto D_e , while M_{ed} is the residual independent of both IOD and ENSO signals. This technique has already been applied successfully in several studies to separate ENSO and IOD signals (e.g. Yu et al. 2005; Izumo et al., 2010; Keerthi et al. 2012; Currie et al. 2013).

2. Model validation

Figure 1 first compares the seasonal variations of equatorial surface currents in the Indian Ocean from both OSCAR currents dataset and model output. OSCAR dataset reveals that fall Wyrтки jet is maximum in November (up to 0.5 m.s^{-1}) in the central IO between 60°E and 80°E (Fig. 1a). The spring Wyrтки jet is maximum in May. This jet is slightly weaker (up to 0.4 m.s^{-1}) and does not last as long as its fall counterpart. These seasonal surface eastward jets occur during the biannual intensification of the equatorial westerly winds and exhibit an apparent westward propagation that has been attributed to a superposition of Rossby waves signature on a wind-forced jet (Nagura and McPhaden 2010b). A period of westerly flow is found during winter in the west of the basin (December-January) while weak currents prevail during the summer season (July-August). As shown on Figure 1b, the model is able to very accurately capture these seasonal features both in terms of seasonal phasing and amplitude, despite a slight eastward surface current bias during winter. The seasonal correlations between model and observed surface currents are highly significant and range between 0.8 and 1 all along the equator strip (not shown).

The mean seasonal cycle of subsurface currents in the equatorial central/eastern IO is further shown on Figure 2 for both RAMA moorings and model outputs. This figure illustrates that, at 80.5°E , the surface jets are generally confined to the upper 60 to 80m of the water column (Fig. 2a). They both exhibit similar maximum amplitude at this location ($\sim 0.5 \text{ m.s}^{-1}$). Further east at 90°E , there is no surface current maximum in fall and the spring jet is less intense. The model is generally able to reproduce these seasonal fluctuations of the surface currents. This figure also reveals periods of transient eastward undercurrents at depth during late summer/early fall (August-October) and late winter/early spring (January-April). The direction of the zonal flow generally reverses during the other seasons. These subsurface currents generally lead the surface signals. The eastward transient undercurrents are even more prominent in the easternmost location (90.5°E ; Fig. 2b), while they tend

to merge with the surface jets in the central IO (at 80°E; Fig. 2a). The model is able to simulate the seasonal occurrence of these seasonal surface jets and undercurrents at both 80.5°E and 90°E (Fig. 2cd against Fig. 2ab). However, it generally tends to slightly overestimate their maximum amplitude and the depth of their maximum is deeper by 30m than in observations. The seasonal correlations between model and observed currents are highly significant and range between 0.8 and 1 at all depth for both locations (not shown). The model also accurately captures the seasonal thermocline variations at both locations (see black contours on Figure 2).

Figure 3 provides a validation of the interannual surface currents variability in the model by displaying the interannual standard deviation of zonal currents in the equatorial IO for both OSCAR and the model outputs (Fig. 3ab) and their corresponding spatial correlation (Fig. 3c). Both datasets show maximum interannual zonal currents variations at the equator between 60 and 90°E. The maximum amplitude of these equatorial currents variations appear to be larger and slightly shifted eastward in the model as compared to OSCAR currents data. Despite these biases, Figure 3c reveals that the model is able to very accurately capture the phasing the interannual variations of surface currents in a broad strip around the equator, with significant correlations generally exceeding 0.7 between 7°N and 7°S. These correlations generally drop down outside this region, with correlation ranging between 0.4 and 0.7.

Interannual variations of vertical current profile along the equator at both 80.5°E and 90°E derived from RAMA moorings and model data are further displayed on Figure 4. The observations exhibit large interannual zonal currents fluctuations both in the surface layers and at depth ranging between -0.7 and 0.7 $\text{m}\cdot\text{s}^{-1}$, an amplitude similar to that of the seasonal cycle (see Figure 2). Interannual currents fluctuations appears to be slightly weaker and more transient at 90°E (Fig. 3b). The model is shown to capture very accurately most of these interannual currents fluctuations at both locations (contours vs. shading on Fig. 4). At 80.5°E, the correlation between interannual zonal currents fluctuations from buoys and model reaches 0.80 in the first 125m and drops down to 0.60 at 150m depth (Fig. 4c). At the easternmost location (90°E), the correlation between model and observations reaches 0.6 from the surface to 200m and then gradually decreases to 0.40 at 250m depth (Fig. 4d). These results clearly demonstrate that the model accurately capture the surface and subsurface currents variations at both seasonal and interannual timescales, giving us confidence in using this dataset to describe the interannual variability of the current system and their relationship with IOD and ENSO variations.

3. General description of interannual currents variations

The general features of the interannual variability of both surface and subsurface currents in the IO are first described performing an Empirical Orthogonal Function (EOF) analysis separately for surface currents in the 10°N-10°S band and for subsurface currents at the equator (Figure 5 and 6 for EOF1 and EOF2 respectively). The first modes of these surface and subsurface EOF analysis represent 23% and 47% of the variance in the horizontal and vertical fields respectively. The left panels of Figure 5 display the main characteristics of the principal components (PC) associated with these EOF analysis. The first striking result is that the PCs of the first EOFs of surface and subsurface interannual currents anomalies are strongly correlated (0.95; Fig. 5a), highlighting that the surface and subsurface currents variations depicted by these first EOFs are related to the same mode of currents variability. In addition, this mode of interannual zonal currents variability is largely representative of the fall season (Fig. 5b), the principal components of these two EOFs exhibiting a maximum amplitude in October-November (~1.4) and far weaker variability in spring (~0.7). Recomputing a similar EOF analysis restricted to the fall season indeed results in similar EOFs patterns (not shown). The right panels of Figure 5 further display the spatial patterns associated with these first EOFs of surface and surface currents. As depicted by the first EOF of current vertical section, this mode of variability exhibits a current dipole along the vertical at the equator (Fig. 5d), with a weak anomalous eastward flow located at depth (100-200m), maximum around 150m located in the central eastern equatorial IO between longitudes 70°E and 90°E, and a strong anomalous westward flow confined to the first 80m and maximum between 65°E and 80°E. As depicted by the first EOF of surface currents, this surface anomalous westward flow is maximum at the equator and confined to the narrow meridional band between 3°N and 5°S, with a maximum amplitude located right at the equator between 65°E and 85°E (shading Fig. 5c), at the same location as the climatological fall Wyrтки jet (contours on Fig. 5c). This mode is hence largely representative of the interannual variability of the fall Wyrтки jet, which is associated at depth with a slight intensification of the eastward subsurface currents when the fall Wyrтки jet weakens (contours on Fig. 5d).

Figure 6 displays the same analysis as Figure 5 but for the second EOFs modes. These second modes capture a weaker percentage of the interannual zonal currents variance, i.e. 7% and 15% for the horizontal and vertical fields respectively. Although to a less extent than the first EOFs, these second surface and subsurface EOFs are also related to each other (Fig. 6a), their respective PCs being correlated at 0.56, suggesting that they also depict a similar mode of zonal current variations. Figure 6b reveals that this mode of current variability is largely representative of the interannual zonal current variations during the spring season, the principal components of these two EOFs

exhibiting a maximum amplitude in December-February (~ 1.3) and far weaker variability in summer and fall. The associated surface pattern exhibit rather weak zonal currents variations at the equator, with an anomalous eastward mainly confined to the western boundary of the basin (Fig. 6c). Larger-scale currents variations occur as an anomalous westward flow south of 2.5°S , maximum between 60°E and 70°E . Consistently with the surface pattern, the associated subsurface pattern exhibits rather weak current anomalies in the upper ocean but larger variations at depth (Fig. 6d), characterized by an subsurface eastward flow upsloping from the western to the eastern part of the basin, with a maximum being located between 150m and 75m depth. These subsurface anomalies occur at the climatological depth of the winter undercurrent (contours on Fig. 6d), further highlighting that this mode is representative of the interannual modulation of the intensity of the winter undercurrent.

Figure 7 further provides the lead-lag correlation between the first and second PCs of both surface and vertical fields. For both surface (Fig. 7a) and vertical section (Fig. 7b), the first mode of zonal current leads the second by about 3-4 months, with a significant correlation of ~ 0.5 and ~ 0.7 for surface and vertical section respectively. This indicates that the fall Wyrтки jet reduction depicted by EOF1 (Fig. 1) is generally followed one season later (i.e. in winter) by the winter EUC intensification depicted by EOF2 (Fig. 6).

To provide a preliminary description of the wind and climate forcing patterns related to the EOFs of surface zonal currents, both SST anomaly and surface wind stress anomaly are regressed onto the principal components of the first two EOFs mode of subsurface zonal currents at the equatorial IO (Fig. 8ab), the first one being representative of the fall Wyrтки jet variability and the second one being representative of the interannual modulation of the intensity of the winter undercurrent. As expected, the anomalous surface near-equatorial westward currents associated with the first surface current mode (Fig. 5c) are associated with strong easterly wind anomalies in the equatorial region (Fig. 8a), suggesting that the surface currents variations depicted by this mode is a direct response to the equatorial wind forcing. A lead-lag correlation between the first principal component of surface zonal current and zonal wind stress further show a maximum correlation of 0.8 between the two PCs, with the currents leading the wind by 1 month (not shown). Nagura and McPhaden (2010a) demonstrated that this current reversal earlier than winds is the consequence of reflected Rossby waves radiating from the eastern boundary. In addition, it can be noticed that the SST signal associated with these equatorial easterly wind anomalies displays a cooling along the west coast of Sumatra and slight warming in the western IO, reminiscent of the IOD signature (Fig. 8a). A similar regression analysis with the second principal component (PC2) of subsurface currents

reveals that the typical SST pattern show that subsurface EOF2 is also reminiscent of the IOD signature (Fig. 8b). This suggest that the main modes of current variations are at least to some extent driven by the IOD related wind forcing.

To better ascertain the relationship between these two modes of equatorial currents variations with both IOD and ENSO climate mode, Figure 8c,d further display a simple lag-correlation analysis of the subsurface PC1 and PC2 onto ENSO and IOD indices described in section 2.2. Figure 8c indicates that IOD exhibits a maximum correlation with PC1 in fall (~ 0.7), suggesting that this mode of variability, peaking in fall, exerts a strong control on the interannual variability of the fall Wyrtki jet. Significant correlations are also evident the preceding summer (~ 0.4) and the following winter (~ -0.4), further demonstrating that the IOD during its onset and demise phase influences to some extent the equatorial surface currents variations. As shown on Figure 8d, the IOD also influences the subsurface currents interannual variations. However, compared to its simultaneous control onto surface currents, the subsurface currents response to IOD is delayed, with a maximum correlation between IOD and PC2 in winter (~ 0.7), i.e. one season after the IOD peak. ENSO also exhibits significant correlations with both PC1 and PC2 (Fig. 8c,d). However, the maximum control of ENSO onto the surface and subsurface currents variability is delayed by one season and slightly weaker (~ 0.6 correlation) as compared to that of the IOD: ENSO exhibits a maximum influence on the surface currents in winter (Fig. 8c) and on the subsurface currents in late winter/early spring (Fig. 8d).

Figure 9 further allows discussing the main mechanisms responsible for subsurface current variations depicted by first two EOFs mode of the vertical currents section at the equator. This Figure shows thermocline (approximated by the 20°C isotherm; upper panels) and wind stress curl and wind stress anomalies (lower panels) regressed into the first two principal components of the vertical EOFs. For both EOFs, the equatorial thermocline anomalies exhibit a zonal dipole pattern, with negative thermocline anomalies in the eastern equatorial IO and positive thermocline anomalies in the western part of the basin (Fig. 9a,b). In agreement with previous studies (e.g. Nyadjro and McPhaden 2014; Zhang et al. 2014), this illustrates that subsurface zonal currents variations at the equator are controlled by zonal pressure gradient variations in the equatorial region as a direct response to equatorial wind anomalies through equatorial waves propagation. In addition to this equatorial response, equatorial subsurface currents variations are also associated with strong thermocline anomalies especially south of equator, with a thermocline deepening extending from 10°S in the central IO westward towards western equatorial IO. The meridional slopes of the regressed thermocline patterns in both hemispheres are consistent with the signature of westward

propagating Rossby waves (Rao and Behera 2005; Yu et al. 2005), with wave signals propagating slower at higher latitudes. As already discussed by Zhang et al. (2014), these deeper thermocline in the west and shallower in the east in both hemispheres indicates a equatorward geostrophic flows converging to the equator. These equatorward geostrophic thermocline flows within the shallow meridional overturning cells feed the zonal flow in the equatorial thermocline, hence contributing to equatorial zonal currents variations at depth. Figure 9c,d further reveals that the strong off-equatorial wind curl signals (around 10°S) are likely to contribute to this off equatorial thermocline deepening signals through Ekman pumping. Our analysis is hence in line with Zhang et al. (2014) who suggested that the interannual variability of zonal currents in the equatorial thermocline is driven by the interannual variability of the equatorial thermocline slope, which results from both equatorial wind anomalies and off-equatorial wind curl anomalies that transmit related off equatorial thermocline signals through the shallow meridional overturning cells. The thermocline and wind patterns shown on Figure 9 are also reminiscent of the signature of IOD but also of ENSO (e.g. Yu and Behara 2005).

As a summary of this section, the analyses presented above demonstrate that the interannual variability of the equatorial currents in the Indian Ocean can be described by two main modes. The first mode exhibits a maximum variability in fall and is typical of a reduction (intensification) of the fall Wyrтки jet associated with an intensification (reduction) at depth. The second mode is maximum in winter and largely describes the interannual variability of the winter EUC, with a weaker surface expression. These two modes can be explained by a combination of both equatorial and off-equatorial wind variations. Our analysis also shows that the second mode tend to lag the first mode by 4-5 months. These two modes are related to the combined influence of co-occurring ENSO and IOD events. However, as already acknowledged in the literature (e.g., Annamalai et al. 2003; Izumo et al. 2013), IOD and ENSO events show a strong tendency to co-occur, our ENSO and IOD indices indeed exhibiting a 0.65 correlation. This co-variability does not allow at this stage to disentangle the respective influence of IOD and ENSO on the variations of the equatorial current system. This is the objective of the following section.

4. Respective influence of IOD and ENSO on equatorial currents variations

The combined influence of IOD and ENSO onto the equatorial current system is first summarized on Figure 10 that shows a simple regression analysis of equatorial currents and zonal winds in the central IO between 65°E and 85°E (i.e. where maximum currents variations are seen for both EOF analysis, see Figs. 5 and 6) onto ENSO and IOD indices. As expected from the tendency from ENSO and IOD events to co-occur, this simple regression display similar regression currents

and wind patterns onto these two indices (compare left and right panels of Figure 10). The combined influence of these two modes results from a strong westward currents anomalies in the surface layers during the fall season indicative of a decrease of fall Wyrтки jet (see climatological currents overlaid as contours on Fig. 10a,c) followed by an eastward currents increase in subsurface from September to March and maximum in December. While the early stage of the subsurface intensification occur near the end of the climatological occurrence of late summer/early fall EUC, the maximum intensification in December occurs when climatological currents at depth are weakest (see climatological currents overlaid as contours on Fig. 10a,c). The co-occurrence of IOD and ENSO are associated with an easterly wind anomalies from August to February (Fig. 10b,d), that directly force the surface fall Wyrтки jet reduction and the subsurface current intensification two months later, i.e. the time it takes for the zonal pressure gradient to equilibrate to the wind forcing through equatorial waves propagation (Chen et al. 2015).

Before separating out the respective influence of ENSO and IOD on the equatorial current system, Figure 11 separates out the respective control of IOD and ENSO onto the wind and thermocline interannual variability in fall, winter and spring but performing a partial regression analysis to extract the influence of IOD independent ENSO and the influence of ENSO independent IOD. The maximum wind response to positive IOD events occurs in boreal fall and is characterized by strong easterlies anomaly in the equatorial region and a positive wind curl signal in the southeastern IO maximum around 8°S (Fig. 11a). The equatorial wind signal drives a thermocline shoaling in the eastern equatorial IO in fall through the generation of an equatorial upwelling Kelvin wave that reflects into a westward propagating upwelling Rossby wave, as illustrated by the two negative thermocline anomalies on either side of the equator in the eastern IO (Fig. 11a). The strong positive wind curl signal in the southeastern IO drives off-equatorial convergence due to Ekman pumping, resulting is a deeper-than-normal thermocline in the central IO in fall. After the IOD demise, IOD related wind signals are considerably weaker (Fig. 11b,c), but the off-equatorial thermocline exhibit an evident westward propagating signal maximum around 8°S in the southern IO from fall until the following spring (Fig. 11a-c), as a result of westward Rossby waves propagation. These positive thermocline anomalies reach the western boundary in late winter.

ENSO-related wind and thermocline patterns differ from those of the IOD (Fig. 11d,e,f). Whereas the IOD-related wind signal dissipates during winter, the ENSO wind signal is maximum during winter (Klein et al., 1999; Xie et al., 2009), one season after the mature phase of the IOD. Similar to IOD, ENSO drive anomalous equatorial easterly winds that persist from fall to spring but with a weaker amplitude than that of the IOD. These easterly anomalies cause a thermocline shoaling

in the eastern equatorial IO maximum in winter (Fig. 11e), while concurrent deepening of the thermocline develops in the southern IO in response to an Ekman pumping signal maximum in winter. These deep thermocline anomalies propagate westwards during spring (Fig. 11f), consistent with a Rossby wave signal, but are weaker and centred further south (around 12°S) than the corresponding IOD anomalies, congruent with the findings of Rao and Behera (2005) and Yu et al. (2005). Because of their slower propagation speed, these anomalies hardly reach the IO western boundary at the end of spring (Fig. 11f). Our results hence indicate a weaker and delayed influence of ENSO on tropical thermocline variations than that of the IOD.

As for the wind and thermocline signals on Figure 11, we separate out the respective influence of ENSO and IOD on the equatorial current system by providing on Figure 12a,d an analysis similar to Figure 10a,c but performing partial regression analysis to extract the influence of IOD independent ENSO and the influence of ENSO independent IOD. This analysis provides a clear picture of the respective influence of these two modes on the equatorial current system. Figure 12a indicates that IOD events are responsible for the surface Wyrтки jet reduction in fall along with the subsurface zonal currents intensification from June to December. These zonal currents signal associated with the IOD are consistent with the IOD-related equatorial wind forcing independent of ENSO (Fig. 12b). As already discussed from Figure 11a-c and consistently with the IOD tendency to peak in fall, maximum equatorial easterly anomalies associated with the IOD are found to occur during that season. As clearly shown on Figure 12b, these easterly wind anomalies are in phase and directly force the fall Wyrтки jet reduction in fall. These easterly wind anomalies also induce a maximum shoaling of the eastern equatorial thermocline in late fall, with a one-month delay typical of Kelvin wave propagation (Fig. 12c). The subsurface currents variations largely mirror the thermocline anomalies, as a direct response to the related change in zonal pressure gradient (Fig. 12c). Indeed, the thermocline shoaling in late fall results in an eastward subsurface current anomalies maximum at $\sim 120\text{m}$ depth (Fig. 12a), maximum one month after the maximum thermocline deepening (Fig. 12c). As a result and in line with Chen et al. (2015), this analysis therefore reveals that the maximum subsurface current intensification occurs 2 months after the maximum surface easterly wind signal. The thermocline deepening and related westward subsurface current anomalies from February onwards (Fig. 12c) are likely to be the result of a downwelling Kelvin wave resulting from the western boundary reflection of the off equatorial Rossby waves south of the equator in winter discussed on Figure 11a-c, rather than a direct response to the equatorial wind forcing which is weak after the IOD demise (Fig. 12b). Finally, the eastward surface currents anomalies in January after the IOD demise (Fig. 12a,b) are likely to result from the combined effect

of the eastward subsurface current surface in early winter and reflected Rossby wave signal at the eastern boundary, rather than a direct response to the surface wind forcing (Fig. 12b).

As already suggested from Figure 8cd, Figure 12d reveals that the impact of ENSO on the equatorial currents is delayed compared to that of the IOD. ENSO related zonal current signature is weak in fall. ENSO signature initiates in winter as a westward surface current anomaly maximum in December that tends to accelerate the demise of the fall Wyrtki jet. ENSO is also responsible for the subsurface current intensification located around 100m depth two to three months later (i.e. from January to April). This intensification occurs at the time of the winter EUC (see climatological currents overlaid as contours on Fig. 11b,d), indicating that ENSO forcing acts to intensify the winter EUC. Once again, these ENSO related zonal currents signature are consistent with the surface wind forcing induced by the remote influence of ENSO. In line with analysis performed on Figure 11, Figure 12e demonstrates that the maximum surface wind signature of ENSO on the IO occurs later than that of the IOD (Fig. 12b), with maximum equatorial easterly wind anomalies spanning from November to March. The maximum amplitude of these anomalies is twice weaker than that of the IOD but last longer. This delayed ENSO signature over the IO extending after the peak of ENSO (i.e. in November) has already been documented and attributed to local air–sea interactions over the Indian Ocean (e.g. Xie et al. 2009). These wind anomalies directly force the westward surface current anomalies seen from November to March (Fig. 12e). These ENSO-related easterly wind anomalies also induce a maximum shoaling of the eastern equatorial thermocline in winter, which drive the EUC intensification in late winter/early spring (Fig. 12f) as a direct response to the related change in zonal pressure gradient. Finally, as compared to those related to the IOD, the off equatorial Rossby waves signals south of the equator related to ENSO (see Fig. 11) are unlikely to play a role on the equatorial thermocline and related subsurface currents variations in winter and spring because of they are emitted at higher latitudes (12°S compared to 8°S in case of IOD) and hence exhibit a weaker propagation speed that do not allow them to reach the western boundary until late spring.

This section hence demonstrates that the first mode of current variability depicted by EOF1 (see Figure 5) is largely driven by IOD wind variations rather than ENSO. Indeed, PC1 averaged in fall exhibit a strong correlation with the IOD index for both surface currents and vertical currents, while the correlations of PC1 with ENSO index are weaker (Fig. 8c,d). Similarly, the strong subsurface current intensification in winter depicted by EOF2 is more controlled by the IOD, although ENSO also significantly contributes to this variability. While ENSO has undoubtedly a weaker and delayed influence on the equatorial current system as compared to the IOD, ENSO

forcing drives the interannual variability of the winter EUC more than the IOD because of its delayed influence on the interannual wind variability as compared to IOD (Fig. 11 and 12).

5. Summary and discussion

5.1. Summary

The observed surface current record derived from satellite data (i.e. OSCAR; Bonjean and Lagerloef 2002) is too short (~20 years) to confidently differentiate the relative contributions of IOD and ENSO to interannual variability because of the strong tendency of these two modes to co-occur. The even shorter observed equatorial currents measurements at depth from ADCP data further prevent a thorough description of the interannual subsurface currents variations in the IO. In this study, we use ~50 years long simulation from an eddy-permitting ($1/4^\circ$) ocean general circulation model forced with realistic interannual air-sea fluxes over the 1958-2007 period to describe the main modes of interannual variability of surface and subsurface equatorial zonal currents in the IO and to separate out the respective contribution of ENSO and IOD on these interannual fluctuations. We first demonstrate that this model simulation accurately captures the surface and subsurface zonal currents variations in the equatorial IO region at both seasonal and interannual timescales, including the variability of the Wyrтки jets derived from satellite data from 1993 and the variability of the seasonally occurring EUCs observed from ADCP from the early 2000.

To provide a general description of the interannual variability of the equatorial current system in the IO, we first perform an EOF analysis of both surface and subsurface zonal current interannual anomalies in the equatorial IO. This analysis reveals two main modes of equatorial currents variability. The dominant mode exhibits a maximum variability in fall and largely describes the variability of the fall Wyrтки jet intensity. The second mode is maximum in winter and largely describes the interannual variability of the subsurface currents in winter, with a weaker surface expression. This winter subsurface current variations depicted by the second mode generally follow the fall Wyrтки jet variability depicted by the first mode by 4 to 5 months.

The surface current variability appears to be directly force by interannual variations of the equatorial zonal winds. These interannual zonal current anomalies at the equator tends to lead the zonal wind stress anomalies by one month, which as been interpreted by Nagura and Mc Phaden (2010a) as a response to the reflected Rossby waves radiating from the eastern boundary. In line with Chen et al. (2015), these equatorial zonal wind variations are further shown to induce anomalous tilt of the equatorial thermocline one season ahead through equatorial wave adjustment that further induce zonal pressure gradient changes and subsurface currents variations. In line with Zhang et al.

(2014), our analysis also show that thermocline depth anomalies south of equator further contribute to zonal currents variations in the equatorial thermocline by through meridional geostrophic flows between the off-equatorial and the equatorial region within the shallow meridional overturning cells. These off-equatorial thermocline signals are driven by a combination of both equatorial Rossby waves induced by equatorial wind signals and off-equatorial Rossby waves induced by off-equatorial wind curl signals.

The SST, wind and thermocline patterns related to these EOF analyses of the equatorial system are reminiscent of the signature of the combined influence of ENSO and IOD over the IO. However, the strong tendency for IOD and ENSO to occur does not allow separating their respective influence. To reach that goal, we further performed partial regression analysis of the equatorial zonal currents that allowed separating ENSO and IOD influence. Our analysis clearly demonstrates that the IOD is largely responsible for the interannual modulation of fall Wyrтки jet intensity by modulating the equatorial wind intensity during that season. The IOD is also responsible for strong subsurface current variations a coupled of months later (around December) induced by the delayed effect of the IOD wind signal onto the equatorial thermocline and related zonal pressure gradient. The equatorial current system response to ENSO is weaker and delayed compared to that of the IOD. The remote and delayed impact of ENSO in the IO induces equatorial wind variations in winter that modulate the surface currents intensity and the intensity of the EUC that seasonally develops during late winter/early spring.

5.2. Discussion

Several previous studies already documented the impact of IOD events of the equatorial current system. Our results confirm previous published literature on the IOD influence on fall surface currents in the equatorial IO (Murtugudde et al. 2000; Vinayachandran et al. 1999, 2002; Grodsky et al. 2001; Han et al. 2004; Nagura and McPhaden 2010a; Gnanaseelan et al. 2012; Nyadjro and McPhaden, 2014), i.e. the intensity reduction (intensification) of the fall Wyrтки surface jet in response to positive (negative) IODs through their control on fall equatorial wind intensity. In agreement with Joseph et al. (2012), our analysis also indicates that IOD events do not affect the intensity of spring Wyrтки jets. Our results also confirm previous published literature on the IOD influence on the equatorial subsurface zonal currents (Iskandar et al. 2009; Nyadjro and McPhaden, 2014; Zhang et al. 2014; Chen et al. 2015), i.e. an anomalous eastward (westward) thermocline flow in late fall/early winter in response to positive (negative) IODs through the delayed response of equatorial thermocline tilt to IOD-related fall equatorial wind variations. Our results further suggest that the maximum subsurface current response to IOD occur in-between the semi-annual EUCs,

suggesting that IOD events only modestly influence the late summer and late winter EUCs intensity. The strong correlations found between the two main modes of equatorial subsurface currents variations in fall and winter and the IOD index (resp. 0.82 and 0.75) further demonstrate that IOD events control most of the equatorial current system variability in these seasons.

Aside from a general description of the interannual variations of the equatorial current system through an EOF analysis, the main originality of the present study has been to assess the specific remote impact of ENSO on the equatorial current system owing the long-term model integration that allowed disentangling the respective influence of the often co-occurring ENSO and IOD events. Because of the delayed ENSO signature in the IO, our results show that ENSO hardly influence the maximum intensity of the fall Wyrтки jet. This result somewhat contradicts results from Gnanaseelan et al. (2012), who suggested that ENSO forcing contribute to the fall Wyrтки jet intensity variations in the eastern part of the basin. We rather find a delayed influence of ENSO, which related winter wind signature that induce surface currents variations during that season. While the IOD influence does not extend into the following year, our results reveal that a significant ENSO influence into the following year, with ENSO forcing modulating the interannual variability of the late winter/early spring EUC induced by the delayed effect of the ENSO wind signal onto the equatorial zonal pressure gradient in that season.

Acknowledgement: Authors acknowledge the Director, National Institute of Oceanography for facility and support. They acknowledge UGC for the financial support given to Chinnu Sachidanandan during the period of study. The authors also acknowledge the DRAKKAR project (<http://www-meom.hmg.inpg.fr/Web/Projets/DRAKKAR/>) for providing the oceanic simulations. Authors are thankful to data management division at National Institute of Oceanography, Goa for providing ADCP data. The authors finally thank the Institut de Recherche pour le Developpement (IRD) for support financially the Indo-French collaboration on Indian Ocean research.

5. References

Akhil VP, F. Durand, M. Lengaigne, J. Vialard, M.G. Keethi, V.V. Gopalakrishna, C. Deltel, F. Papa, C. de Boyer Montégut, 2014 : A modeling study of the processes of surface salinity seasonal cycle in the Bay of Bengal, *JGR-Ocean*, 116, 3926-3947, doi : 10.1002/2013JC009632

Akhil VP, M. Lengaigne, J. Vialard, F. Durand, M.G. Keerthi, A.V.S. Chaitanya, F. Papa, V.V. Gopalakrishna, C. de Boyer Montégut, 2016: A modelling study of processes controlling the Bay of Bengal seasurface salinity interannual variability, accepted to *JGR*

Anderson, D. L. T., and D. J. Carrington (1993) Modeling interannual variability in the IO using momentum fluxes from the operational weather analyses of the United Kingdom Meteorological Office and European Centre for Medium-Range Weather Forecasts., *J. Geophys. Res.*, 98, 12483–

12499, doi: 10.1029/93JC00407.

Annamalai H, Murtugudde R, Potemra J, Xie SP, Liu P, Wang B (2003) Coupled dynamics in the Indian Ocean: spring initiation of the zonal mode. *Deep-Sea Res* 50B:2305–2330

Bonjean, F., and G. S. E. Lagerloef (2002) Diagnostic model and analysis of the surface currents in the tropical Pacific Ocean, *J. Phys. Oceanogr.*, 32, 2938–2954.

Brodeau L, Barnier B, Treguier AM, Penduff T, Gulev S (2010) An ERA 40-based atmospheric forcing for global ocean circulation models. *Sci Direct* 31:88–104. doi:10.1016/j.ocemod.2009.10.005

Bruce, J (1973) Equatorial undercurrent in the western Indian Ocean during the southwest monsoon. *J. Geophys. Res.*, 78,6386–6394, doi:10.1029/JC078i027p06386.

Cane, M. A. (1980), On the dynamics of equatorial currents, with application to the Indian Ocean, *Deep Sea Res., Part A*, 27, 525–544, doi:10.1016/0198-0149(80)90038-2.^{[[SEP]]}

Chu, P. C. (2010), Observational studies on association between eastward equatorial jet and Indian Ocean dipole, *J. Oceanogr.*, 66(3), 429–434.

Clark, A.J., and Liu, X (1993) Observations and dynamics of semiannual and annual sea levels near the eastern equatorial Indian Ocean boundary, *J. Phys. Oceanogr.*,23,386-399.

Chen, G., W. Han, Y. Li, D. Wang, and M. McPhaden (2015) Seasonal-to-Interannual Time Scale Dynamics of the Equatorial Undercurrent in the Indian Ocean, *J. Phys. Oceanogr.*, 45, 1532-1553, doi: <http://dx.doi.org/10.1175/JPO-D-14-0225.1>.

Currie JC, Lengaigne M, Vialard J, Kaplan, D. M., Aumont, O., Naqvi, S. W. A., and Maury, O.: Indian Ocean Dipole and El Niño/Southern Oscillation impacts on regional chlorophyll anomalies in the Indian Ocean, *Biogeosciences*, 10, 6677-6698, doi:10.5194/bg-10-6677-2013, 2013.

Du, Y., Xie, S.-P., Huang, G., and Hu, K.: Role of air– sea interaction in the long persistence of El Niño–induced north Indian Ocean warming, *J. Climate*, 22, 2023–2038, doi:10.1175/2008JCLI2590.1, 2009.

Gnanaseelan, C., Deshpande, A., McPhaden, M. J (2012) Impact of Indian Ocean Dipole and El Niño/Southern Oscillation wind-forcing on the Wyrki jets, *J. Geophys. Res.*, 117, C08005, 2012

Grotsky, S. A., J. A. Carton, R., Murthugudde (2001) Anomalous surface currents in the tropical Indian Ocean, *Geophys. Res. Lett.*, 28, No.22, 4207-4210.

Han, W., and J. P. McCreary (1999) Dynamics of the eastern surface jets in the equatorial Indian Ocean, *J. Phys. Oceanogr.*, 29, 2191-2209.

Han, W., P.J. Webster, R. Lukas, P. Hacker, and A. Hu (2004) Impact of atmospheric intraseasonal variability in the Indian Ocean: low-frequency rectification in equatorial surface current and transport., *J. Phys. Oceanogr.*, 34, 1350-1372.

Izumo, T., J. Vialard, M. Lengaigne, C. de Boyer Montégut, S. K. Behera, J-J. Luo, S. Cravatte, S. Masson and T. Yamagata, 2010 : Influence of the Indian Ocean Dipole on following year’s El Niño, *Nature Geoscience*, 3, 168-172.

Izumo, T., M. Lengaigne, J. Vialard, G. Madec, S. K. Behera and T. Yamagata, 2013: Influence of Indian Ocean Dipole and Pacific recharge on following year's El Niño: interdecadal robustness, *Climate Dynamics*, 42, 291–310, doi :10.1007/s00382-012-1628-1

Iskander, I., I., Masumoto, Y., and Mizuno, K (2009) Dynamics of wind forced intraseasonal zonal current variations in the equatorial Indian Ocean, *J. Geophys. Res.*, 116, C06019.

Joseph S, Wallcraft AJ, Jensen TG, et al (2012) Weakening of spring Wyrтки jets in the Indian Ocean during 2006–2011. *Journal of Geophysical Research: Oceans* (1978–2012) 117:n/a–n/a. doi: 10.1029/2011JC007581

Keerthi MG, Lengaigne M, Vialard J, de Boyer Montegut C, Muraleedharan PM (2013) Interannual variability of the Tropical Indian Ocean mixed layer depth., *Clim Dyn* 40:743–759.

Keerthi MG, M. Lengaigne, K. Drushka, J. Vialard, C. de Boyer Montegut, M. Levy, P.M. Muraleedharan, 2016: Intraseasonal variations of the mixed layer depth in the Indian Ocean, 46(7), 2633–2655, doi: 10.1007/s00382-015-2721-z.

Klein SA, Soden BJ, Lau NC (1999) Remote sea surface temperature variations during ENSO: evidence for a tropical atmospheric bridge. *J Clim* 12:917–932

Knauss, J. A., and B. A. Taft (1964) Equatorial Undercurrent of the IO. *Science*, 143, 354–356, doi:10.1126/science.143.3604.354.

Krishnan, R., and P. Swapna (2009) Significant influence of the boreal summer monsoon flow on the Indian Ocean response during dipole events. *J. Climate.*, 22, 5611–5634, doi: 10.1175/2009JCLI2176.1.

Levitus, S. (1998) Climatological atlas of the world ocean, Tech. Rep. 13, NOAA, Silver Spring, Md.

Luo J-J, Zhang R, Behera S, Masumoto Y, Jin F-F, Lukas R, Yamagata T (2010) Interaction between El Niño and extreme Indian Ocean Dipole. *J Clim* 23:726–742

McPhaden, M. J. (1982), Variability in the central equatorial Indian Ocean. Part I: Ocean dynamics, *J. Mar. Res.*, 40, 157–176.

McPhaden, M. J., Y. Wang, and M. Ravichandran (2015), Volume transports of the Wyrтки jets and their relationship to the Indian Ocean Dipole, *J. Geophys. Res. Oceans*, 120, 5302–5317, doi:10.1002/2015JC010901.

Molinari, R. L., D. Olson, and G. Reverdin (1990) Surface current distributions in the tropical Indian Ocean derived from compilations of surface buoy trajectories, *J. Geophys. Res.*, 95, 7217–7238.

Murthugudde, R., J. P. McCreary and A.J. Busalachi (2000) Oceanic processes associated with anomalous events in Indian Ocean relevance to 1997–98, *J. Geophys. Res.*, 105, 3295–3306.

Nagura, M., and M. J. McPhaden (2010a) Dynamics of zonal current variations associated with the Indian Ocean dipole, *J. Geophys. Res.*, 115, 11026, doi:10.1029/2010JC006423.

Nagura, M., and M. J. McPhaden (2010b), Wyrтки jet dynamics: Seasonal variability, *J. Geophys. Res.*, 115, C07009, doi:10.1029/2009JC005922.

- Nidheesh AG, Lengaigne M, Unnikrishnan AS, Vialard J (2013) Decadal and long-term sea level variability in the tropical Indo-Pacific, *Clim Dyn.*, doi:10.1007/s00382-012-1463-4.
- Nyadjro, E., and M. J. McPhaden (2014) Variability of zonal currents in the eastern equatorial Indian Ocean on seasonal to interannual time scales. *J. Geophys. Res. Oceans*, 119, 7969–7986, doi: 10.1002/2014JC010380.
- O'Brien, J.J. And H.E.Hurlburt (1974) Equatorial jet in the Indian Ocean: theory. *Science*, 184, 1075-1077.
- Qiu, Y., L.Li, and W.Yu (2009) Behaviour of the Wyrтки jet observed with surface drifting buoys and satellite altimeter, *Geophys. Res. Lett.*, 36, L18609.
- Rao, S. A., and S. K. Behera (2005) Subsurface influence on SST in the tropical Indian Ocean: Structure and interannual variability, *Dynam.Atmos.Ocean*, 39,103-135.
- Reppin, J., F. A. Schott, and J. Fischer (1999) Equatorial currents and transports in the upper central Indian Ocean: Annual cycle and Interannual variability, *J. Geophys. Res.*, 104(C7), 15495-15514.
- Rayner, N. A.; Parker, D. E.; Horton, E. B.; Folland, C. K.; Alexander, L. V.; Rowell, D. P.; Kent, E. C.; Kaplan, A (2003) Global analyses of sea surface temperature, sea ice, and night marine air temperature since the late nineteenth century, *J. Geophys. Res.*, Vol. 108, No. D14, 440710.1029/2002JD002670.
- Saji, N.H., B.N.Goswami., P.N.Vinayachandran, and T.Yamagata (1999) A dipole mode in the tropical Indian Ocean, *Nature*, 401,360-363.
- Schott, F. A., and J. P. McCreary (2002) The monsoon circulation of the Indian Ocean, *Progress in Oceanography*, 51, 1–123.
- Schott, F. A., S.-P. Xie, and J. P. McCreary Jr. (2009), Indian Ocean circulation and climate variability, *Rev. Geophys.*, 47, RG1002, doi:10.1029/2007RG000245. [L_{SEP}]
- Swallow, J (1964) Equatorial Undercurrent in the western Indian Ocean. *Nature*, 204, 436–437, doi: 10.1038/204436a0.
- Swapna, P., and R. Krishnan (2008) Equatorial undercurrents associated with Indian Ocean dipole events during contrasting summer monsoons., *Geophys. Res. Lett.*, 35, L14S04, doi: 10.1029/2008GL033430.
- Thompson B, Gnanaseelan C and P. S. Salvekar (2006) Variability in the Indian Ocean circulation and salinity and its impact on SST anomalies during dipole events. *Journal of Marine Research*, 64, 853– 880, doi: 10.1357/002224006779698350
- Uppala SM et al (2005) The ERA-40 re-analysis. *Q J R Meteorol Soc* 131:2961–3012
- Vialard J, Drushka K, Bellenger H, Lengaigne M, Pous S, Duvel JP (2013) Understanding Madden–Julian induced sea surface temperature variations in the North Western Australian basin. *Clim Dyn* 41(11–12):3203–3218
- Vinayachandran, P.N., N.H.Saji, and T.Yamagata (1999) Response of the equatorial Indian Ocean to an unusual wind event during 1994, *Geophys. Res. Lett.*, 26(11), 1613-1616.

- Vinayachandran, P.N., S. Iizuka and T. Yamagata (2002) Indian Ocean Dipole mode events in an ocean general circulation model, *Deep Sea Res., Part II*, 49, 1573-1596.
- Vinayachandran, P. N., J. Kurian, and C. P. Neema (2007) Indian Ocean response to anomalous conditions in 2006, *Geophys. Res. Lett.*, 34, L15602, doi: 10.1029/2007GL030194.
- Webster, P.J., A.W. Moore, J.P. Loschnigg, and R.R. Leben (1999) Coupled ocean-atmosphere dynamics in the IO during 1997-1998, *Nature*, 401, 356-360.
- Wyrtki, K. (1973) An equatorial jet in the Indian Ocean, *Science*, 181, 262-264.
- Xie S-P, Hu K, Hafner J, Tokinaga H, Du Y, Huang G, Sampe T (2009) Indian Ocean capacitor effect on Indo-western Pacific climate during the summer following El Niño. *J Clim* 22:730–747
- Yu, W., B. Xiang, L. Liu, and N. Liu (2005) Understanding the origins of interannual thermocline variations in the tropical IO, *Geophys. Res. Lett.*, 32, L24706.
- Yuan, D., and W. Han (2006) Roles of equatorial waves and western boundary reflection in the seasonal circulation of the equatorial Indian Ocean, *J. Phys. Oceanogr.*, 36, 930–944.
- Zhang Y.C., Rossow W.B., Lacis A.A., Oinas V., Mishchenko M.I (2004) Calculation of radiative fluxes from the surface to top of atmosphere based on ISCCP and other global data sets refinements of the radiative transfer model and the input data, *J. Geophys. Res.*, 109, 27.
- Zhang D, McPhaden MJ, Lee T (2014) Observed interannual variability of zonal currents in the equatorial Indian Ocean thermocline and their relation to Indian Ocean Dipole. *Geophys Res Lett* 41:7933–7941. doi: 10.1002/2014GL061449.

Seasonal equatorial zonal currents and winds

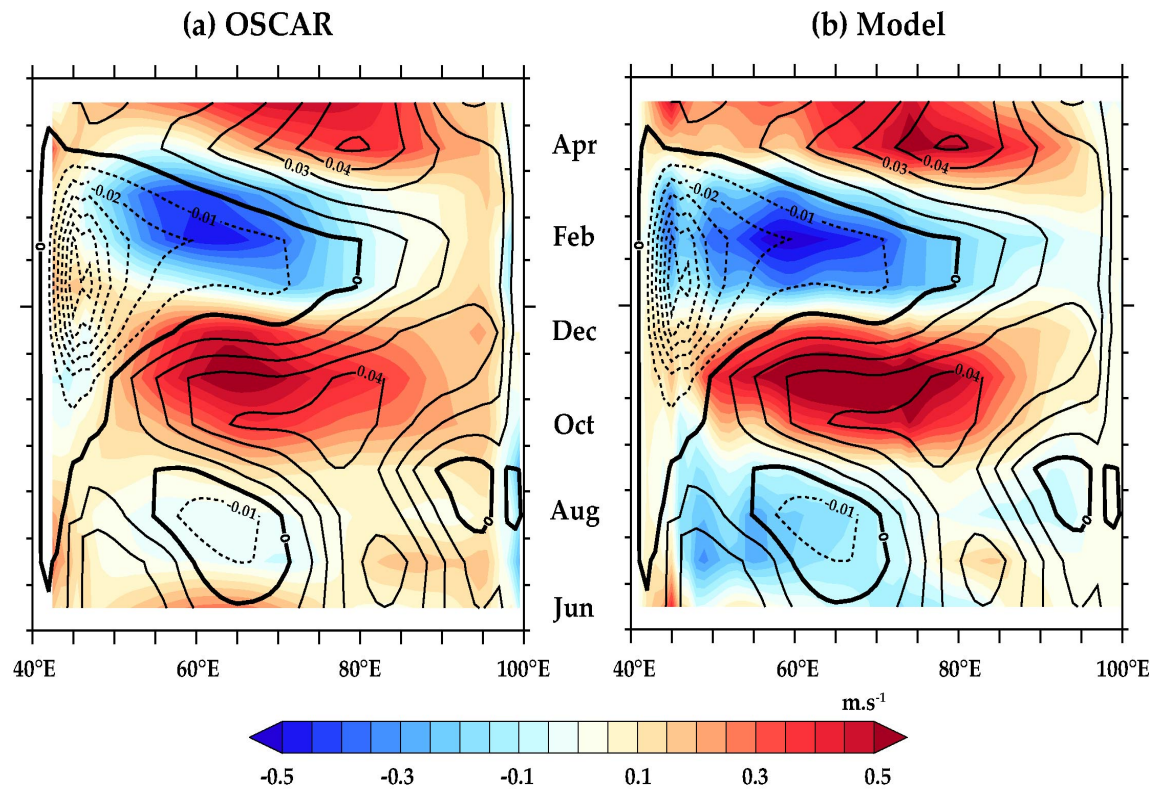


Figure 1. Longitude-time evolution of seasonal climatology of equatorial zonal surface currents from (a) OSCAR dataset and (b) model outputs. The corresponding zonal wind stress climatology from the model is overlaid on each panel. These climatologies are computed over the common 1993-2007 period. Units are in m.s^{-1} for currents and N.m^{-2} for wind stresses.

Seasonal equatorial zonal currents

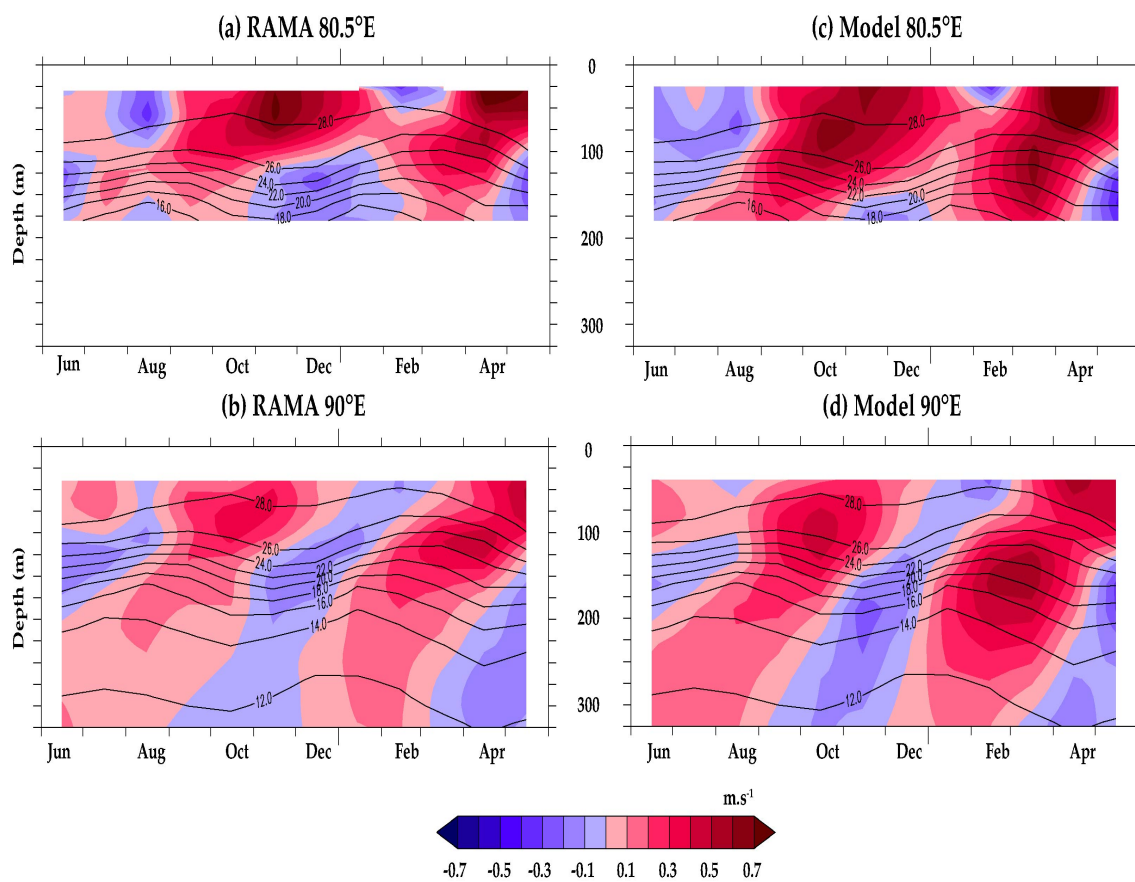


Figure 2. Vertical section of seasonal equatorial zonal currents (color) and temperature (contour) at (left) 80.5°E and (right) 90°E from (top) RAMA moorings and (bottom) model output. Seasonal climatologies are calculated from November 2004 to December 2007 at 80.5°E and from November 2000 to December 2007 at 90°E for both datasets. Units are in m.s^{-1} .

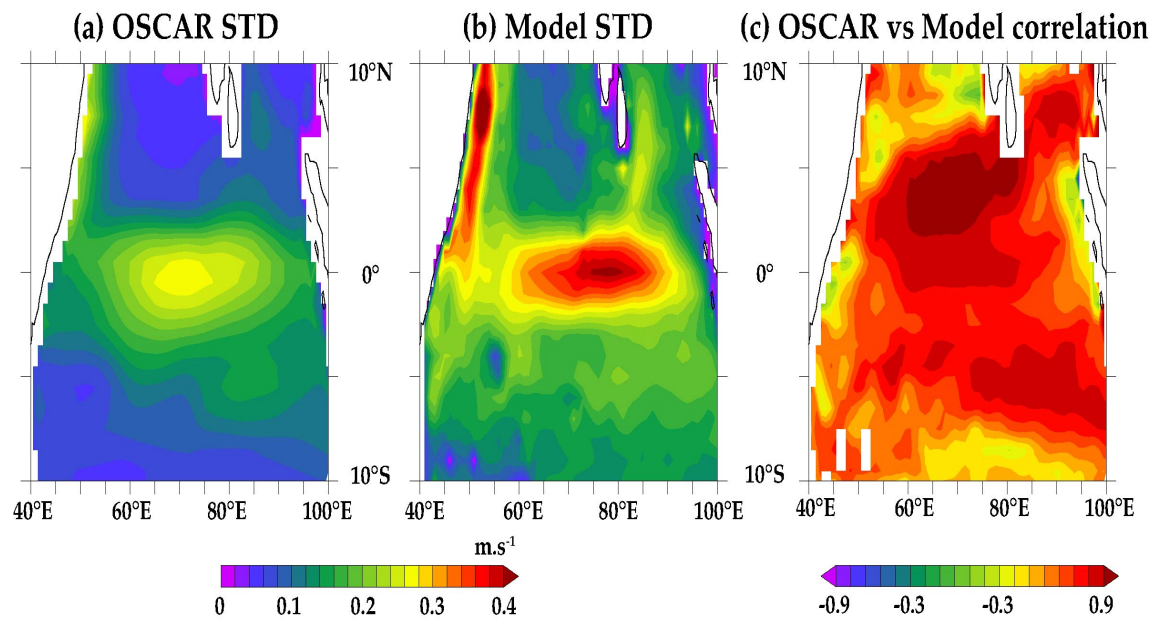


Figure 3. Standard deviation maps of interannual zonal surface currents from (a) OSCAR dataset (b) model output. (c) Correlation maps between interannual zonal current anomalies derived from OSCAR and model outputs. Interannual anomalies from both datasets are calculated over the 1993-2007 period.

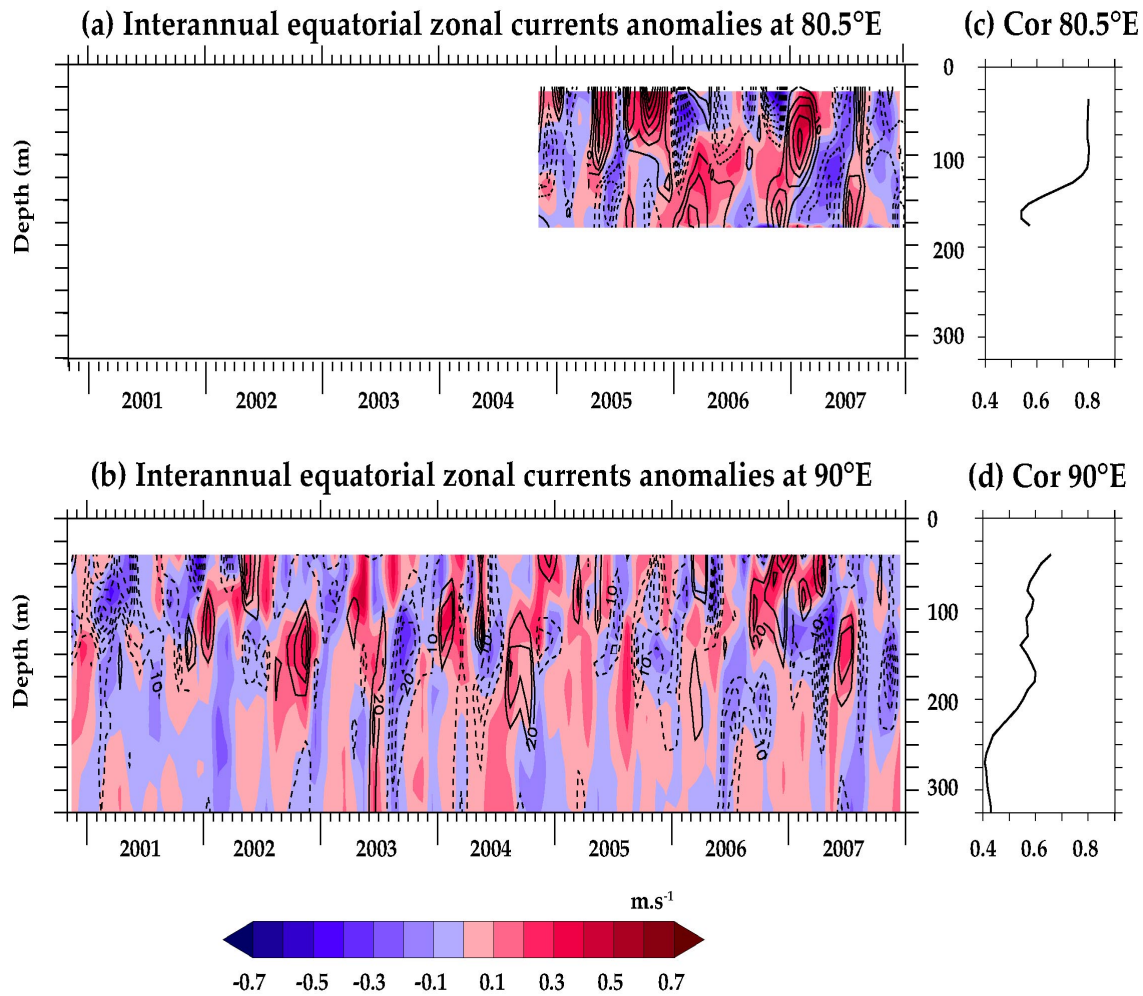


Figure 4. Interannual anomalies of equatorial zonal currents at **(a)** 80.5°E and **(b)** 90°E from RAMA buoys (shaded) and simulation (contour). Corresponding correlations between modelled and observed interannual anomalies of equatorial zonal currents at **(c)** 80.5°E and **(d)** 90°E. Anomalies are calculated from their respective monthly climatology (October 2004 to December 2007 at 80.5°E and November 2000 to December 2007 at 90°E location).

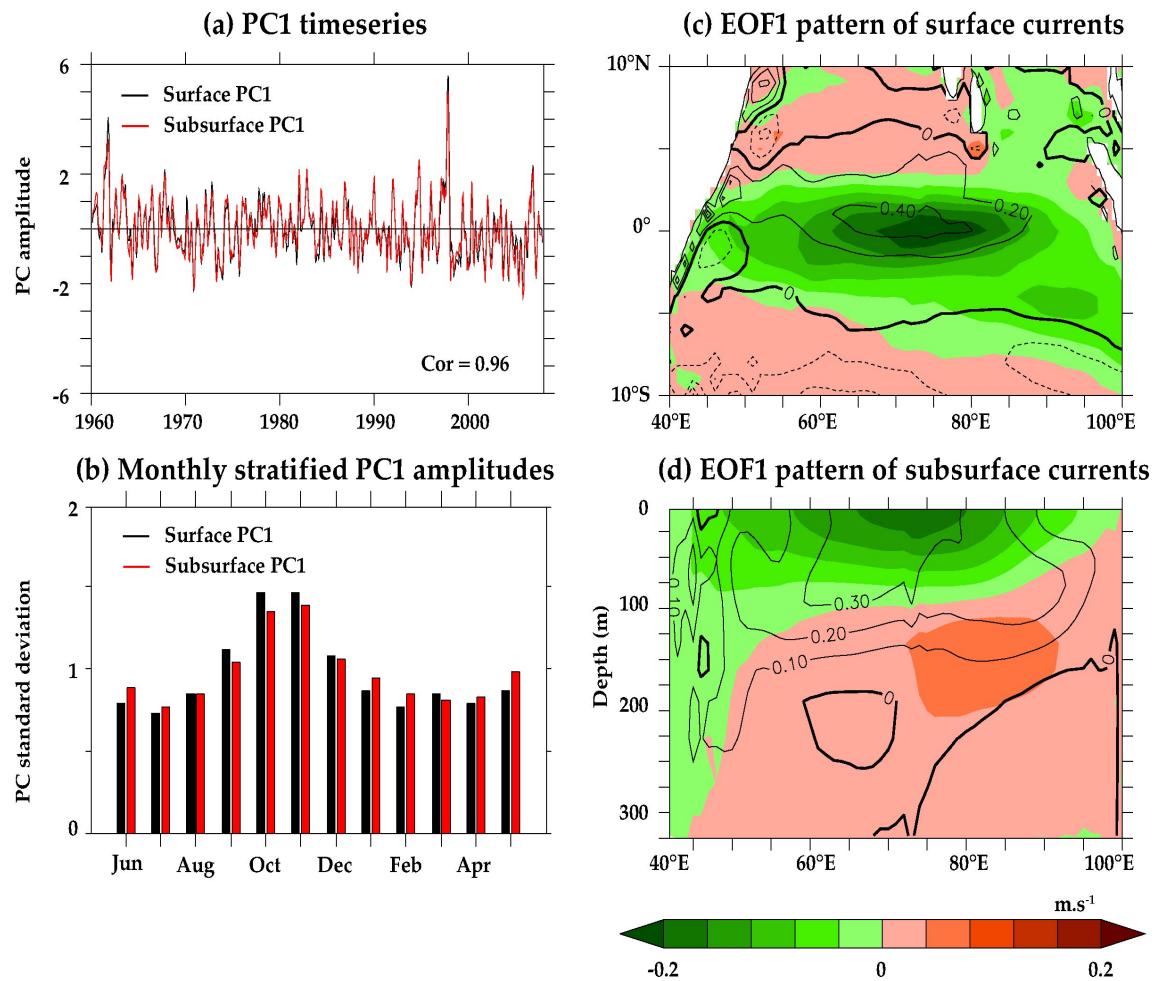


Figure 5. (a) Timeseries and (b) monthly standard deviation of normalized principal components of the first EOF of interannual surface zonal currents anomalies (black) and equatorial vertical section of interannual zonal currents anomalies (red) from the model over the 1960-2007 period. The correlation between the two principal components is indicated on panel a. Corresponding first EOF pattern of (c) surface zonal currents anomalies and (d) equatorial vertical sections of zonal currents anomalies. Climatological fall currents (September-November) are overlaid on panels c and d.

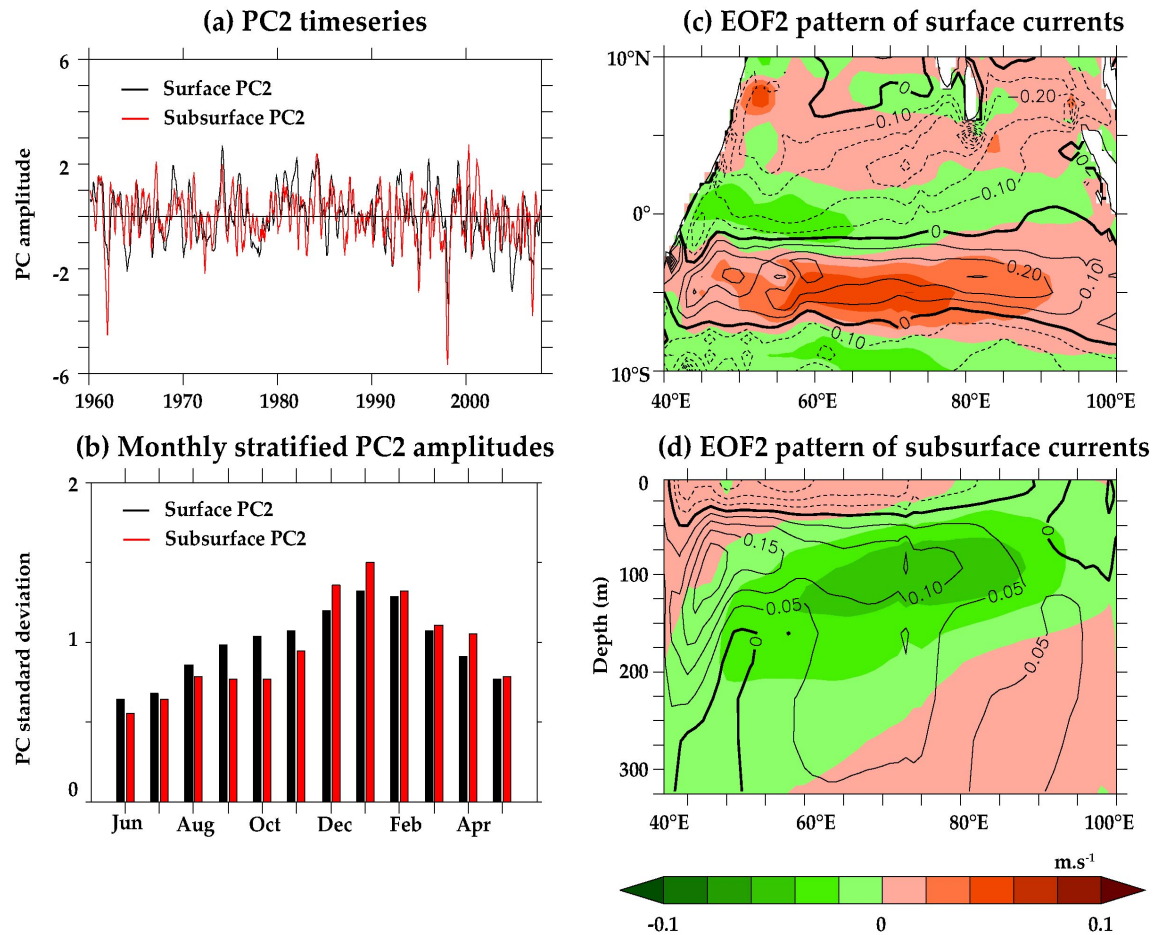


Figure 6. (a) Timeseries and (b) monthly standard deviation of normalized principal components of the second EOF of interannual surface zonal currents anomalies (black) and equatorial vertical section of interannual zonal currents anomalies (red) from the model over the 1960-2007 period. The correlation between the two principal components is indicated on panel a. Corresponding second EOF pattern of (c) surface zonal currents anomalies and (d) equatorial vertical sections of zonal currents anomalies. Climatological winter currents (December-February) are overlaid on panels c and d.

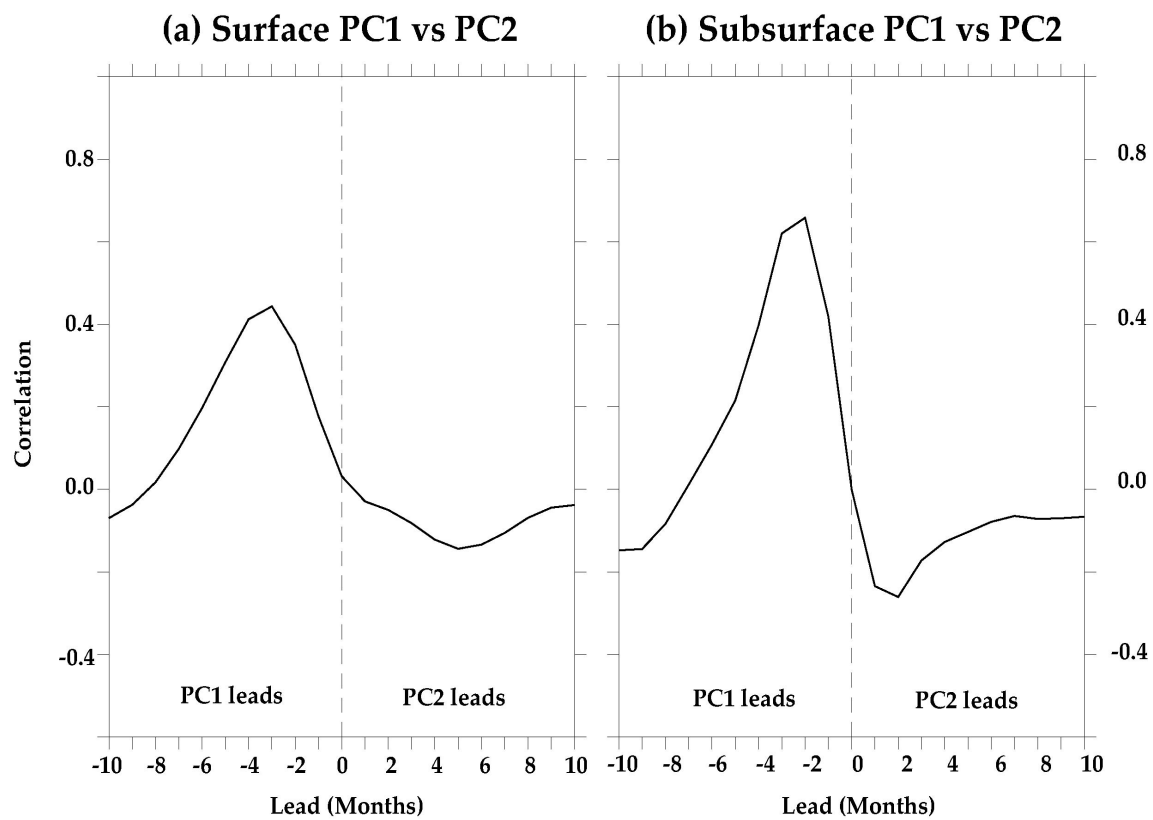


Figure 7. Lag correlation of the principal components of EOF1 and EOF2 of (a) surface and (b) equatorial vertical section of interannual zonal currents anomalies.

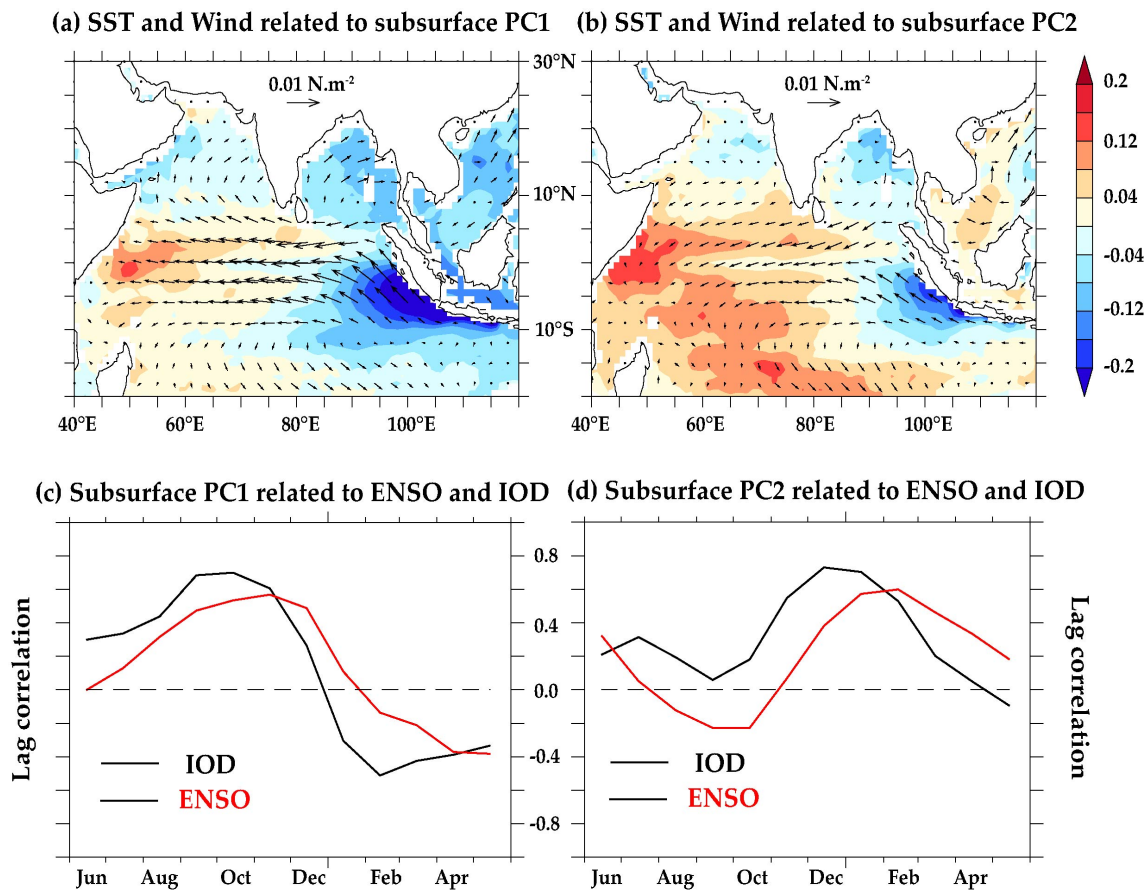


Figure 8. Sea surface temperature (shaded) and wind stress anomalies (vectors) regressed onto of the principal components of (a) EOF1 and (b) EOF2 of the equatorial vertical section of interannual zonal currents anomalies. Simple lag-correlation of (c) PC1 and (d) PC2 of equatorial vertical section of interannual zonal currents anomalies onto IOD (black lines) and ENSO (red lines) indices over the 1960-2007 period.

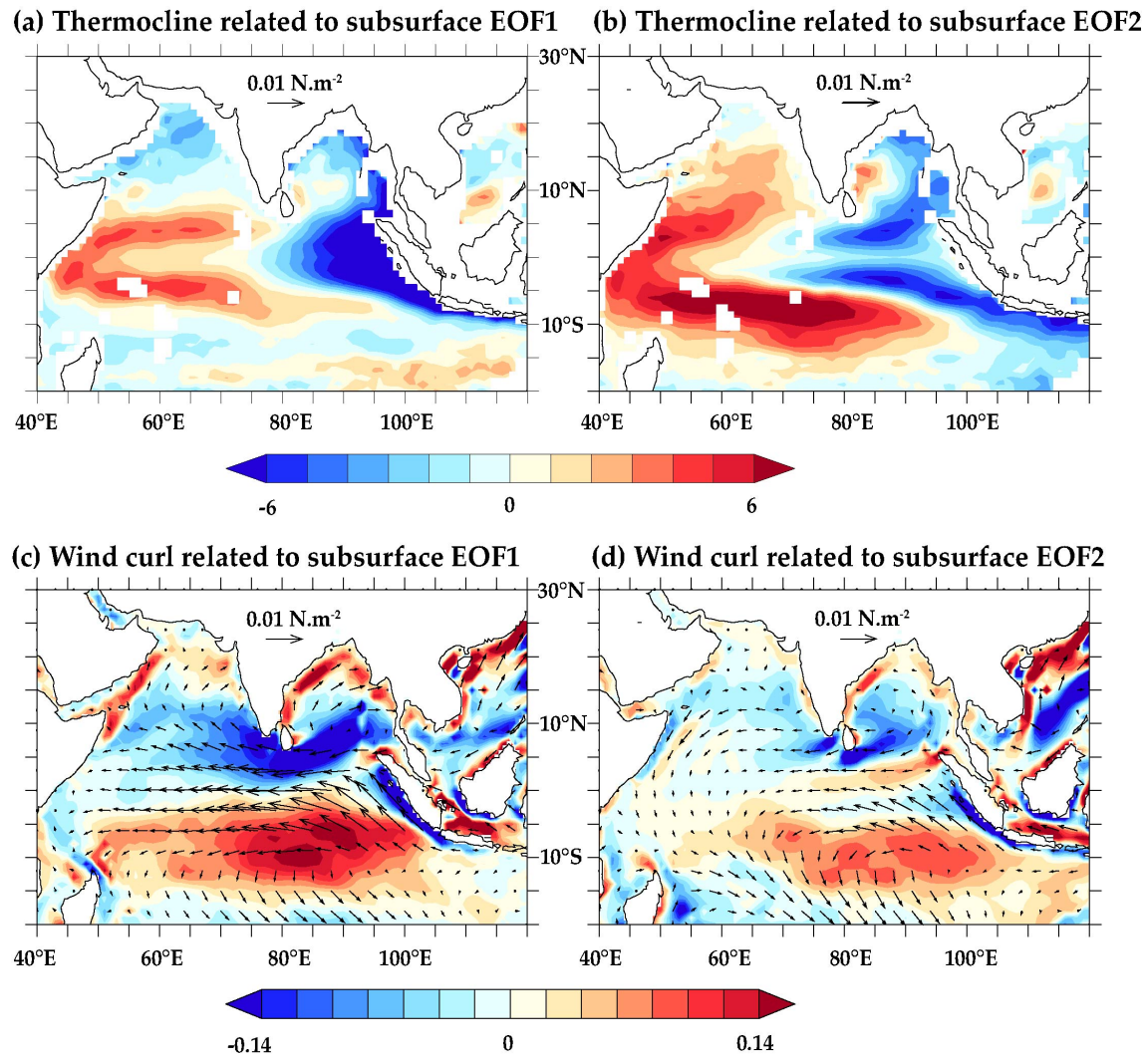


Figure 9. 20°C isotherm depth anomalies regressed onto the principal components of (a) EOF1 and (b) EOF2 of interannual equatorial subsurface zonal currents analysis. (c-d) Same as (a-b) but for wind stress curl (shading) and wind stress (vectors) anomalies.

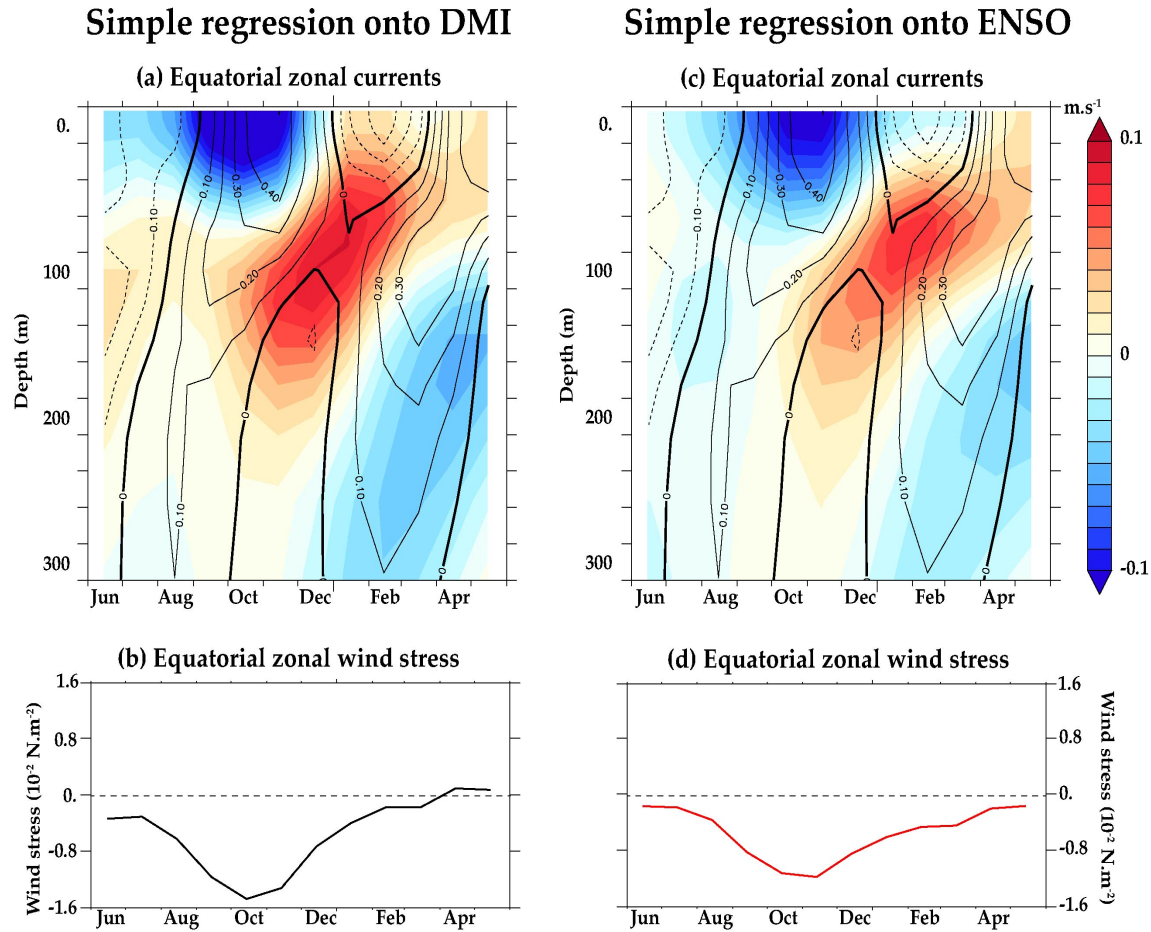


Figure 10. Simple regression of **(top)** vertical section of zonal currents and **(bottom)** equatorial zonal winds averaged over the $[2^{\circ}\text{N}-2^{\circ}\text{S}; 65^{\circ}\text{E}-85^{\circ}\text{E}]$ region onto **(left)** DMI index and **(right)** ENSO index over the 1960-2007 period. Corresponding vertical sections of climatological zonal currents are overlaid on panels b and d.

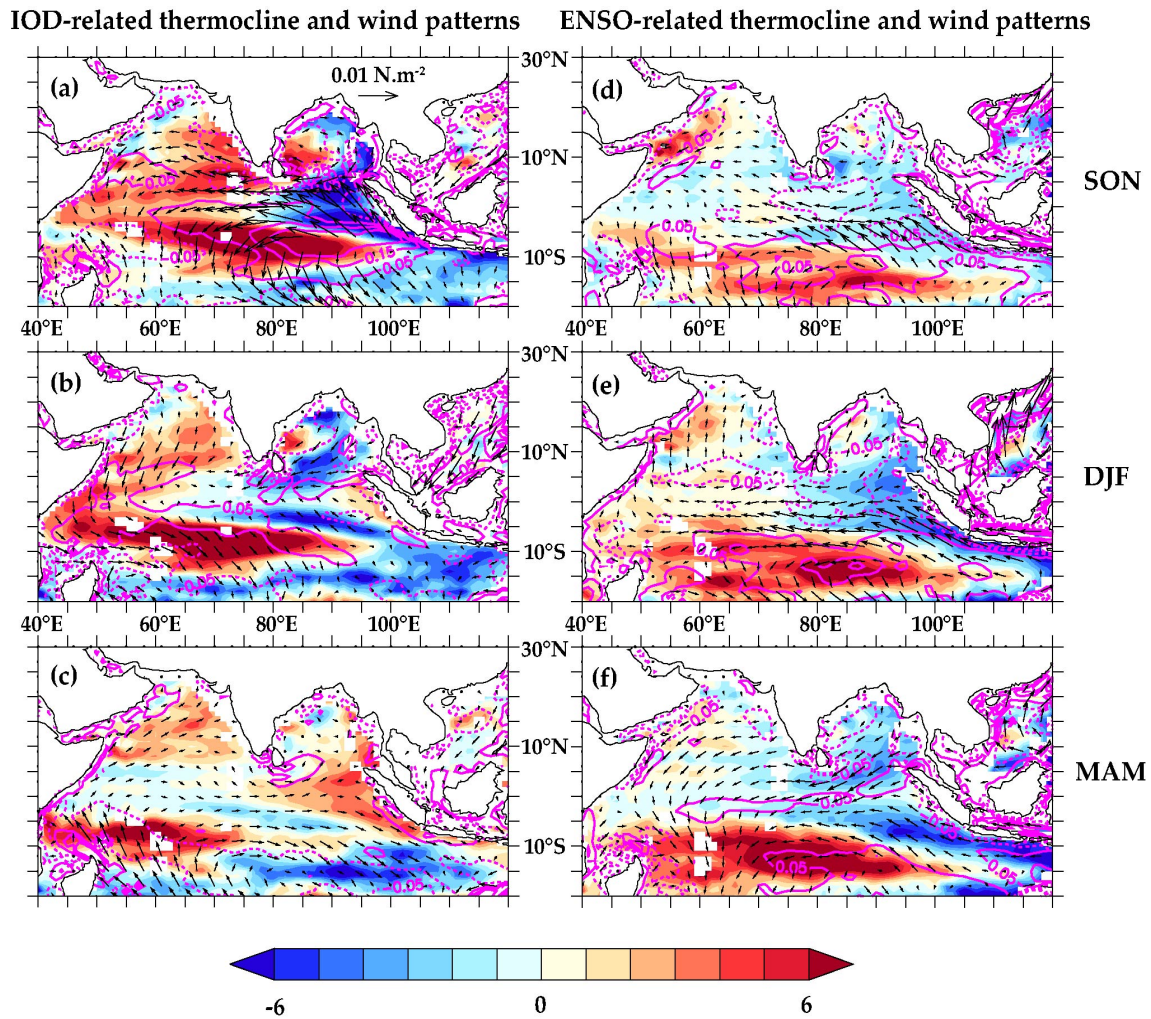


Figure 11. Partial regression of 20°C isotherm depth anomalies (colour), wind stress curl (contour) and wind stress (vector) onto **(left)** DMI index with the influence of ENSO index removed and **(right)** ENSO index with the influence of the DMI index removed over the 1960-2007 period for **(top)** fall (SON), **(middle)** winter (DJF) and **(bottom)** spring (MAM). Wind curl contour are in 10^{-7} N.m⁻³.

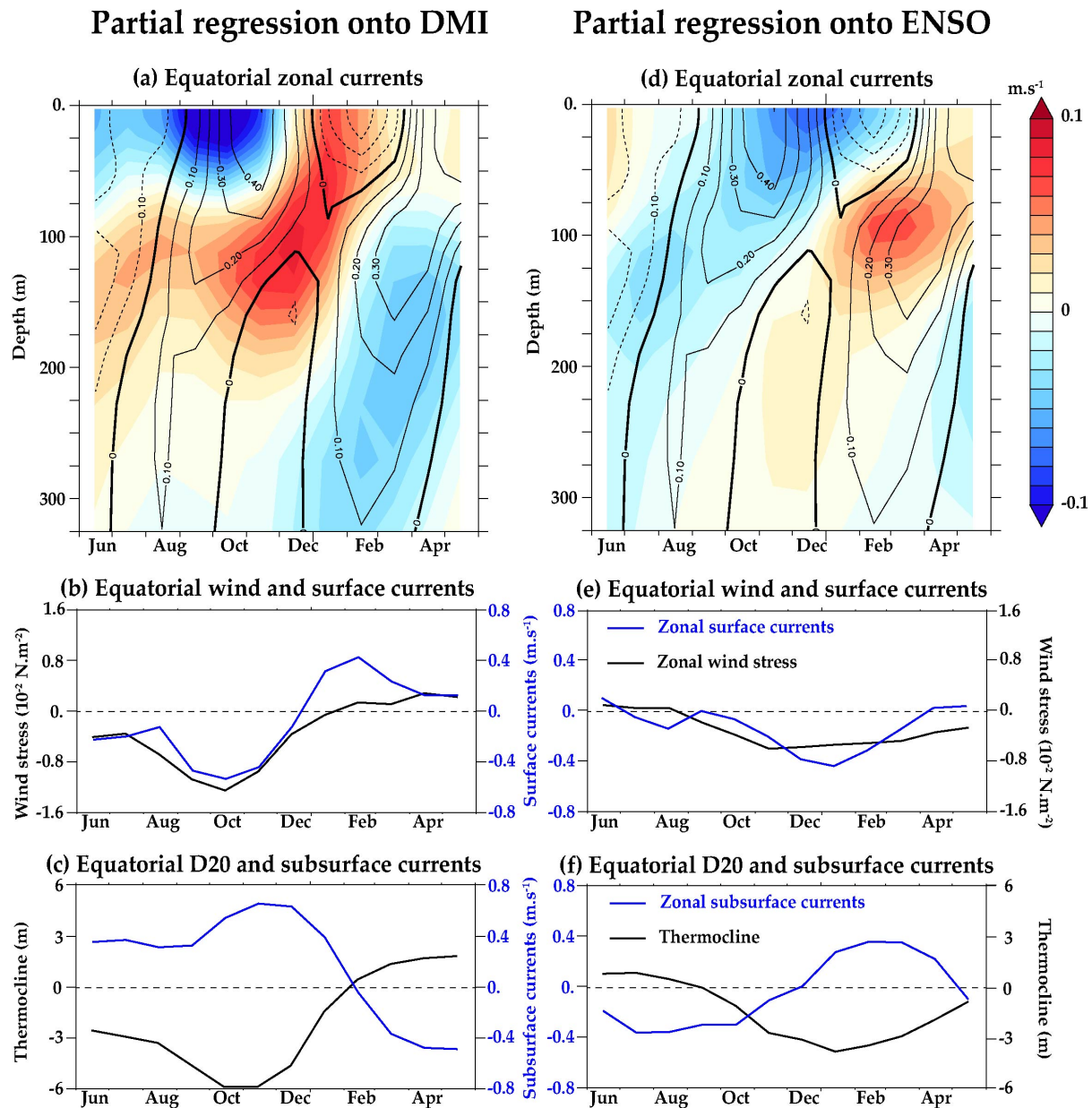


Figure 12. Partial regression of **(top)** vertical section of zonal currents, **(middle)** equatorial zonal winds (black) and zonal surface currents averaged over the $[2^{\circ}\text{N}-2^{\circ}\text{S}; 65^{\circ}\text{E}-85^{\circ}\text{E}]$ region (blue), **(bottom)** zonal subsurface currents averaged over the $[2^{\circ}\text{N}-2^{\circ}\text{S}; 65^{\circ}\text{E}-85^{\circ}\text{E}; 80\text{m}-180\text{m}]$ region (blue) and equatorial thermocline averaged over the $[5^{\circ}\text{N}-5^{\circ}\text{S}; 80^{\circ}\text{E}-100^{\circ}\text{E}]$ region (black) onto **(left)** DMI index with the influence of ENSO index removed and **(right)** ENSO index with the influence of the DMI index removed over the 1960-2007 period. Corresponding vertical sections of climatological zonal currents are overlaid on panels a and b.